THE TOTAL MASS AND THE GAS FRACTION IN X-RAY GALAXY CLUSTERS: DO WE REALLY KNOW WHAT WE MEASURE ?

Stefano Ettori

INAF, Osservatorio Astronomico di Bologna, Italy

ABSTRACT

I present recent work done to study (1) the systematics that affect the total cluster mass measurements through X-ray analysis and (2) the distribution of baryons in simulated X-ray galaxy clusters.

Key words: X-rays: galaxies: clusters; dark matter; galaxies: clusters.

1. INTRODUCTION

My quick answer to the provocative question in the title is **yes**. I will discuss more extensively on the systematics that affect the total mass and the gas mass fraction measurements obtained through X-ray studies.

2. SYSTEMATICS IN THE X-RAY CLUSTER MASS ESTIMATORS

This work is done in collaboration with Elena Rasia, Lauro Moscardini, Pasquale Mazzotta and others (Rasia, Ettori et al. 2005, MNRAS, submitted). We examine the systematics affecting the X-ray total mass estimators applied to a set of five galaxy clusters resolved at high resolution in hydrodynamic simulations, including cooling, star formation and feedback activities and assuming the standard ΛCDM cosmological model (see Borgani et al. 2004). The simulation has been carried out with the parallel Trees-PH simulation code GADGET-2 (Springel 2005). A first cluster of our sample (C_{Pert}) is directly extracted from the final output of this simulation by using the standard identification criteria based on the spherical over-density. The remaining four objects have been instead obtained by re-simulating at high-resolution galaxy clusters selected from the same simulation. The new initial conditions for these runs have been generated by applying the Zoomed Initial Condition technique (Tormen et al. 1997). This method allows to increase the mass resolution in a suitably chosen high–resolution Lagrangian region surrounding the structure to be re–simulated, and at the same time to correctly describe the large–scale tidal field of the cosmological environment by using low–resolution particles. Notice that we performed a series of DM–only runs to create initial conditions which produce clusters that, at $z = 0$, are not affected by contamination from low-resolution particles out to (4–6) virial radii. These initial conditions, suitably adapted to include the gas component, have been used to obtain the high–resolution re–simulations corresponding to the galaxy clusters C_{Merg}, C_{Rel1}, C_{Rel2} and C_{z05}. To summarize, the following five objects have been selected as examples of clusters with different thermal and dynamic state: C_{Pert} ($T_{\rm sl} = 3.9$ keV, $M_{\rm vir} = 7.0 \times 10^{14}\, M_\odot$), a perturbed cluster which shows in the temperature map a cold substructure infalling toward the center; C_{Merg} ($T_{\rm sl} = 3.6$ keV, $M_{\rm vir} = 4.1 \times 10^{14}\, M_\odot$), an object that experienced a recent major merger; C_{Rel1} ($T_{\rm sl} = 3.3$ keV, $M_{\rm vir} = 3.6 \times 10^{14}\, M_\odot$), a relaxed structure (see Fig. 1; C_{Rel2} ($T_{\rm sl} = 2.7$ keV, $M_{\rm vir} = 2.3 \times 10^{14}\, M_\odot$), a colder relaxed cluster; C_{z05} ($T_{\rm sl} = 2.8$ keV, $M_{\rm vir} = 2.6 \times 10^{14}\, M_\odot$), a medium–temperature cluster at redshift of 0.5 that corresponds to the most massive progenitor of C_{Rel1}.

We obtain mock *Chandra* ACIS-S3 observations of the simulated objects through the X-ray Map Simulator, *X-MAS* (Gardini et al. 2004). This software is constituted from two main units: a *first unit* uses as input the output of a hydro-N-body simulation. For each gas particle, the emissivity is computed and distributed over the corresponding volume. After selecting a line of sight for the simulated observation, (i) the projected spectrum for each pixel and, then, (ii) the differential flux for each angular coordinate in bins of energy are computed. The final step is to add the Galactic absorption. A *second unit* estimates the expected number counts and iteratively subdivide the tile region until the counts become smaller than a given threshold (10 counts). The `XSPEC` command `FAKEIT` is then used to convolve the spectral model of each subregion with the response of the CCD and to add the sky background. A final photon event file is then generated and analyzed with standard tools, like CIAO and `XSPEC`, as done for real observations. Since we want to study the systematic discrepancies between observed and real quantities for ideal observations, we have applied very long exposure times to all the simulated observations aiming to minimize the statistical uncertainties related to the number counts: 1 Msec for C_{Pert}, C_{Merg}, C_{Rel1} and C_{Rel2}, and 1.5 Msec for C_{z05}.

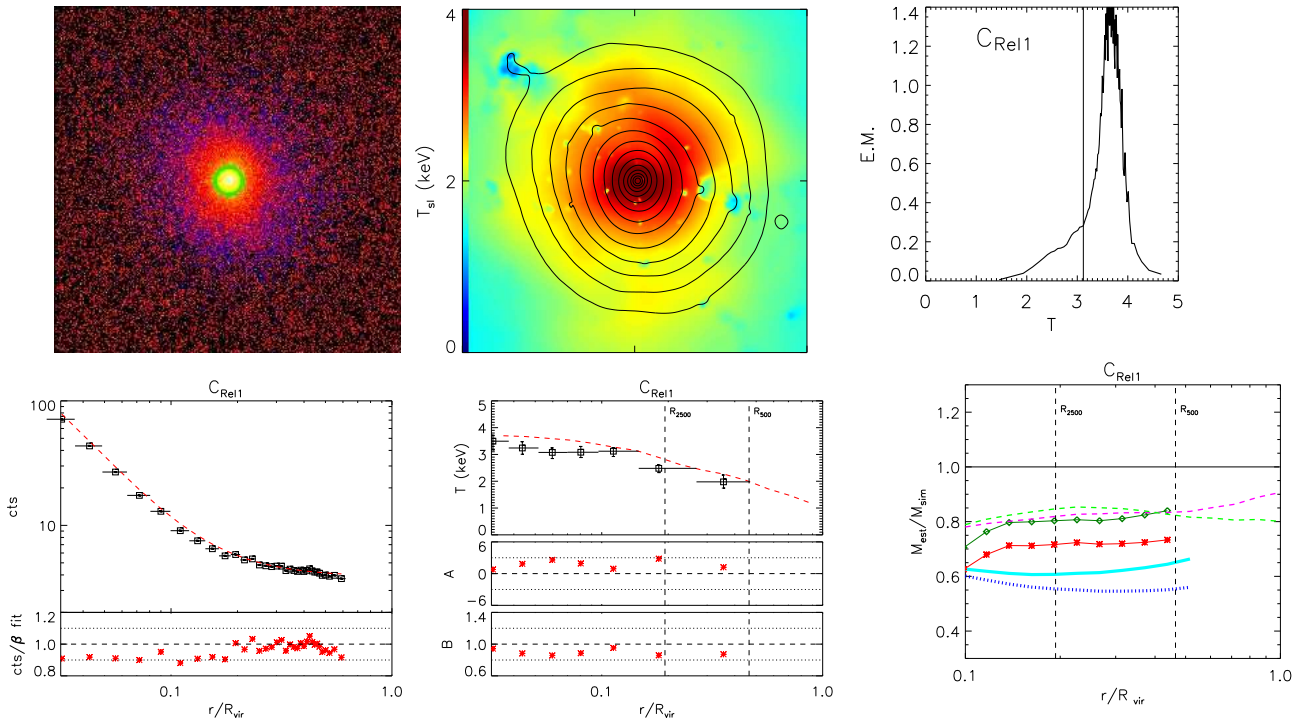

Figure 1. Results for C_{Rel1}. From top-left to bottom-right: (a) photon images in the X-ray soft [0.5-2 keV] energy band The images are 8.3 arcmin-width, exposure-corrected, and binned to $2''$–pixel. The green circles show the regions masked out in the analysis. (b) X-ray logarithmic isoflux contours over-plotted to the spectroscopic-like temperature map, both extracted directly from the hydrodynamic simulations; the temperature scale is shown on the left. (c) Emission measure from region inside R_{500}. The solid vertical black line refers to T_{500}. (d) The surface brightness profile (in units of photon counts) of the simulated cluster C_{Rel1}. Open squares represent the values extracted from the X-ray analysis, the horizontal bars correspond to the bin sizes. The solid curve is the corresponding best-fit β-model, with $\beta = 0.52$ and $r_c = 22$ kpc (= 0.014 $R_{\rm vir}$). The bottom panel shows the ratio between the profile from the X-ray analysis and the best-fit β-model. (e) Deprojected temperature profile. The dashed line represents the profile for the three-dimensional mass-weighted temperature $T_{\rm mw}$ as obtained from the hydrodynamic simulation. The open squares are the values extracted from the X-ray analysis, the vertical bars are 1σ errors ($\sigma_{\rm spec}$), while the horizontal ones correspond to the bin sizes. The bottom graphs in each panel show quantities related to the differences between the two temperatures: $A \equiv (T - T_{\rm mw})/\sigma_{\rm spec}$ and $B \equiv (T/T_{\rm mw})$. The dotted lines indicate $A = (-3, 3)$ and $B = (0.8, 1.2)$. (f) Ratios between the mass profiles derived from the X-ray analysis, $M_{\rm est}$, and the true mass profile of the simulated cluster, $M_{\rm sim}$. The vertical lines indicate R_{500} and R_{2500}. Total mass estimates: red asterisks = M_{HE}, green diamonds = $M_{HE,v}$, solid cyan line = M_β, dotted blue line = $M_{\beta,\gamma}$, green dashed line = $M_{\rm NFW}$, magenta dashed line = $M_{\rm RTM}$.

2.1. X-ray analysis

The surface brightness profiles have been extracted from [0.5-5 keV] images that have been corrected by the corresponding exposure maps. The profiles are build by considering annuli centered on the minimum of the cluster potential well (which is always off-set from the X-ray peak by less than 2 arcsec) and requiring a fixed number of counts per bin (between 2,500 and 10,000). These azimuthally-averaged profiles are then fitted with a β-model.

The overall temperature is measured in spectra extracted from circular regions centered on the cluster center and with $r = R_{500}$. The temperature profiles are measured in spectra extracted from the same annular regions used in the spatial analysis. For each region, the ancillary response file (ARF) and the redistribution matrix file (RMF), weighted by the X-ray brightness in the [0.3–2 keV] energy range, are computed by using the CIAO tools `mkwarf` and `mkrmf`. Source spectra are extracted from the event file, re-binned to have a minimum of 20 counts per bin and analyzed in the [0.6–7 keV] band. Background spectra are extracted from the background event file for the same source regions. A thermal model (`mekal`) absorbed by the Galactic column density is fitted to the data by using the χ^2 statistic in `XSPEC`. The only free parameters are the gas temperature and the normalization, being Galactic absorption $N_{\rm H}$, redshift z and metallicity Z fixed to the input values adopted in the *X-MAS* run: $N_{\rm H} = 5 \times 10^{20}$ cm^{-2}, $z = 0.175$ (or 0.5 in the case of C_{z05}) and $Z = 0.3 Z_{\odot}$.

To compute the mass through the equation of the hydrostatic equilibrium, we need to recover the three-dimensional profiles of the gas temperature and density by deprojecting the quantities measured in the X-ray spectral analysis. We adopt the deprojection technique presented in Ettori et al. (2002). In Fig.1, we compare the deprojected temperature measurements in C_{Rel1}, T, with the three-dimensional mass-weighted estimates, $T_{\rm mw} = \int mTdV / \int mdV$ with m being the mass of each gas particle, as obtained from the simulations. $T_{\rm mw}$ is the proper value that one should use in the hydrostatic equilibrium equation to measure the mass. Note that its profile is in remarkable good agreement with the deprojected spectral one, since the cluster in exam has a quite azimuthally symmetric thermal structure.

2.2. X-ray estimates of the gravitational mass

The "true" mass profile, $M_{\rm sim}(< r)$, of the simulated objects, obtained by summing all the masses of the particles inside a sphere of radius r, can be now compared to several different X-ray mass estimators, $M_{\rm est}$: (1) $M_{\rm HE}$ and $M_{\rm HE,v}$ from the direct application of the hydrostatic equilibrium (HE) equation neglecting and including contributions from the gas motion, respectively; (2) $M_{\beta,\gamma}$ by using a $\beta-$model and both an isothermal ($\gamma = 1$) and polytropic temperature profile; (3) $M_{\rm NFW}$ and $M_{\rm RTM}$ by assuming the analytic mass models in Navarro, Frenk & White (1995) and Rasia, Tormen & Moscardini (2004), respectively, that, combined with the deprojected gas density profile, enable us to recover a temperature profile through the numerical inversion of the HE equation that is then fitted to the observed profile (see Fig. 1).

We find that the main sources of the discrepancy are, in decreasing order of significance, (i) the neglected contribution from the gas motions to the energy budget, (ii) the bias in the X-ray temperature measurements, (iii) the poor determination of the parameters describing the spatially-extended X-ray emission, (iv) a temperature profile assumed to be inappropriately either constant or described by a polytropic relation. In particular, about half of the total error budget of the discrepancy between the true mass and the mass derived from the hydrostatic equilibrium equation is provided from neglecting the kinetic energy still present as bulk motions of the intra-cluster medium. The poorness of the $\beta-$model in describing the gas density profile makes the evaluated masses to be underestimated by ~ 35 per cent with respect to the true mass, both with an isothermal and a polytropic temperature profile. We conclude that the most robust way to recover through X-ray analysis the input radial mass distribution is to adopt an analytic mass model, such as the above-mentioned NFW and RTM, and fit the temperature profile expected from the hydrostatic equilibrium equation to the observed one over a sufficiently large (i.e. $r > R_{500}$) radial range.

3. THE BARYON FRACTION IN SIMULATED GALAXIES CLUSTERS

In this work, Klaus Dolag, Stefano Borgani, Giuseppe Murante and I (Ettori et al. 2005, MNRAS, submitted, astro-ph/0509024) study the baryon mass fraction in a set of hydrodynamical simulations of galaxy clusters performed using the Tree+SPH code `GADGET-2` (Springel 2005) that includes an entropy-conserving formulation of SPH, radiative cooling, heating by a UV background, and a treatment of star formation and feedback from galactic winds powered by supernova explosions. The purpose of the present work is to use an extended set of hydrodynamical simulations of galaxy clusters, treating a variety of physical processes, to study how the spatial distribution of the baryons, as contributed from both the stellar component and the hot X-ray emitting gas, are affected by the physical conditions within clusters at different redshift. The following physical schemes are considered: *Gravitational heating only (code=G)*; *Gravitational heating only with low viscosity scheme (code=GV)*, where an alternative implementation of artificial viscosity is used and clusters are found to have up to 30 per cent of their thermal energy in the turbulent motion of the ICM; *Cooling + Star Formation + Feedback with weak winds (code=FwW)*, where the wind speed is fixed at ≈340 km s^{-1}; *Cooling + Star Formation + Feedback with weak winds and Conduction (code=FwWC)*, where the conduction efficiency is set to be $1/3$ of the Spitzer rate; *Cooling + Star Formation + Feedback with no winds (code=F)*, that is like *FwW*, but with winds switched off;

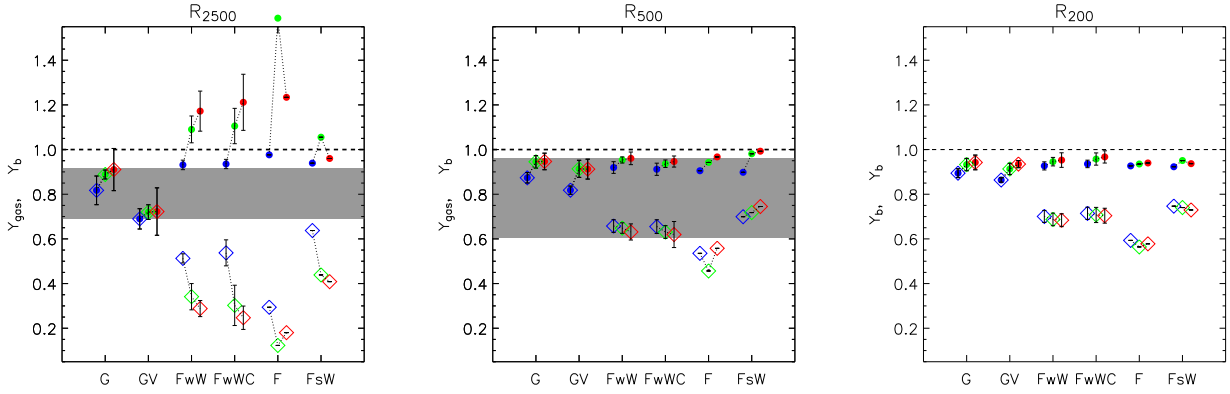

Figure 2. The gas (diamonds) and total baryon (dots) mass fractions, in unit of the cosmic baryonic value at R_{2500} (left panel), R_{500} (central panel) and R_{200} (right panel). For each physical case considered, we plot the mean and standard deviation values measured at $z = 0$, 0.7 and 1. The shaded region show the error-weighted mean and standard deviation of (1) $f_{\rm gas}(R_{2500})$ estimated from 26 X-ray luminous galaxy clusters in Allen et al. (2004, quoted in Table 2 for a LCDM universe), (2) $f_{\rm gas}(R_{500})$ from 35 highly luminous ($L_{\rm X} > 10^{45}$ erg s^{-1}) objects in Ettori & Fabian (1999). The observational data are normalized to $\Omega_{\rm b}h^2 = 0.0214 \pm 0.0020$ (Kirkman et al. 2003), $H_0 = 70$ km s^{-1} Mpc^{-1} and $\Omega_{\rm m} = 0.3$.

Cooling + Star Formation + Feedback with strong winds (code=FsW), where the winds have a speed of ≈480 km s^{-1}, corresponding to a supernova efficiency of unity.

We consider two sets of clusters, which have been selected from different parent cosmological boxes. The first set is extracted from the large–scale cosmological simulation presented in Borgani et al. (2004). The second one is a re-simulation of 9 galaxy clusters, extracted from a pre-existing lower–resolution DM–only simulation. The center of each cluster is defined as the position of the particle having the minimum value of the gravitational potential. Starting from this position, we run a spherical overdensity algorithm to find the radius R_{Δ_c} encompassing a given overdensity Δ_c, with respect to the critical one at the redshift under exam, and the mass M_{Δ_c} enclosed within this radius. In the present work, we consider values of the overdensity Δ_c equal to 2500, 500 and 200. The corresponding radii relate to the virial radius, which defines a sphere with virial overdensity (of $\approx$ 101 at $z = 0$ and $\approx$ 157 at $z = 1$ for our cosmological model and with respect to the critical value), as $(R_{2500}, R_{500}, R_{200}) \approx (0.2, 0.5, 0.7) \times R_{\rm vir}$. For each cluster, the hot gas mass fraction and the stellar mass fraction within a given radius r are then calculated as $f_{\rm gas}(< r) = M_{\rm gas}(< r)/M_{\rm tot}(< r)$ and $f_{\rm star}(< r) = M_{\rm star}(< r)/M_{\rm tot}(< r)$, respectively.

For the sake of clarity, we define the quantities $Y_{\rm gas}$, $Y_{\rm star}$ and $Y_{\rm b}$ as the ratios between $f_{\rm gas}$, $f_{\rm star}$ and $f_{\rm b} = f_{\rm gas} + f_{\rm star}$, and the cosmic value adopted in the present simulations, $\Omega_{\rm b}/\Omega_{\rm m} = 0.13$. The quantities $Y_{\rm gas}$ and $Y_{\rm b}$ at R_{2500}, R_{500} and R_{200}, as a function of redshift and physics included in the simulations, are plotted in Fig. 2. In the inner cluster regions, the dissipative action of radiative cooling enhances the average $Y_{\rm b}$ to super-cosmic values at high redshift. At late times cooling is less efficient, and $Y_{\rm b}$ declines, although to values (~ 0.9 at $z = 0$) that remain higher than those of the non-radiative runs. A smaller scatter and more widespread agreement among the different physical regimes are instead found in the outskirts ($r \approx R_{500}$ and above). The gas fraction within R_{2500} is about 0.3 times the cosmic value at $z = 1$ and 0.6 at $z = 0$, whereas is more tightly distributed around $0.6 - 0.7$ at larger radii, with evidence of larger values in the presence of strong winds. We also compare in Fig. 2 our simulation results with the observed $f_{\rm gas}$ distribution in highly X-ray luminous clusters. Simulations clearly indicate a sizeable underestimate of the hot baryons budget, both at R_{2500} and at R_{500}. When extra physics is added to the action of gravitational heating, lower hot gas fractions result. The discrepancy with the inferred observed fraction signals the existence of systematic errors, either in our physical treatment, or in estimates of the observed fraction, or possibly both. It is worth noticing that total mass estimates, for instance, suffer from systematic differences when measured from X-ray analysis and from dark matter particles in simulations, mainly owing to bias in the X-ray spectral temperature measurements (see, e.g., Mazzotta et al. 2004 and, specifically related to the systematics in X-ray mass estimates, Rasia et al. 2005 and previous section).

As for the cluster set extracted from a cosmological box, which are simulated by including cooling, star formation and feedback with weak (340 km s^{-1}) winds, we find at R_{200} $Y_{\rm b} = 0.93$, $Y_{\rm gas} = 0.74$ and $Y_{\rm star} = 0.20$, with scatter around these values of 2, 4 and 8 per cent, respectively. These results are virtually independent of the cluster mass over the range $M_{\rm vir} \approx (0.5-13) \times 10^{14} h^{-1} M_\odot$. The dispersion relative to the mean value measured at R_{2500} is a factor of about 3 larger than R_{200}.

In the four massive ($M_{200} > 10^{15} h^{-1} M_\odot$) galaxy clus-

ters simulated with 6 different physical schemes, we find that the cosmic value of the baryon fraction $\Omega_{\rm b}/\Omega_{\rm m}$ is reached at about $3 \times R_{200}$. The gas fraction increases radially, reaching 50 (80) per cent of the value measured at R_{200} at $r \approx 0.1(0.3)R_{200}$ at $z = 0$. At $z = 1$ the same values are reached at radii which are about 40 per cent larger. This indicates that $f_{\rm gas}$ tends to be less concentrated at higher redshift, where the more efficient star formation causes a more efficient removal of gas from the hot phase in the central cluster regions. We also find that in these clusters the amount of hot baryons, in unit of the cosmic value, is less scattered and less dependent on the particular physics adopted when it is measured over larger cluster regions. In the runs with *Gravitational heating only*, $Y_{\rm b} = f_{\rm bar}/(\Omega_{\rm b}/\Omega_{\rm m})$ ranges between 0.82 ± 0.06 (at R_{2500}) and 0.89 ± 0.02 (at R_{200}) at $z = 0$. It increases at $z = 1$ to 0.91 ± 0.10, 0.95 ± 0.04 and 0.94 ± 0.03 at R_{2500}, R_{500} and R_{200}, respectively.

3.1. Implications for the constraints on cosmological parameters

Our results have a direct implication on the systematics that affect the constraints on the cosmological parameters obtained through the cluster baryon mass fraction (e.g. White et al. 1993, Ettori 2003, Allen et al. 2004 and references therein). We remind that, once a representative gas fraction, denoted here $\hat{f}_{\rm gas}$, is directly measured from X-ray observations and a statistical relation between the average $\hat{f}_{\rm star}$ and $\hat{f}_{\rm gas}$ is adopted, the cosmic mass density parameter can be then evaluated as

$$\Omega_{\rm m} = \frac{Y_{\rm b}\ \Omega_{\rm b}}{\hat{f}_{\rm gas}\left(1 + \hat{f}_{\rm star}/\hat{f}_{\rm gas}\right)}, \qquad (1)$$

where the "hat" indicates the observed quantities and the cosmic baryon density $\Omega_{\rm b}$ is assumed from primordial nucleosynthesis calculations or the measured anisotropies in the cosmic microwave background. In recent years this method has been also extended to the measure of the dark energy density parameters (Ω_Λ, w; see, e.g., Ettori et al. 2003, Allen et al. 2004) under the assumption that the gas fraction remains constant in redshift (Sasaki 1996). Since the gas fraction scales with the angular diameter distance as $f_{\rm gas} \propto d_{\rm A}^{1.5}$, the best choice of cosmological parameters is defined as the set of values that minimizes the χ^2 distribution of the measured gas fraction at different redshifts.

Despite its conceptual simplicity and straightforward application, this method makes some assumptions that have to be tested before the error bars estimated for the matter and dark–energy density parameters can be accepted as robust and reliable determination of both statistical and systematic uncertainties. In the present discussion, we highlight two of the assumptions generally adopted, but never verified: (1) the mean value of $Y_{\rm b}$ does not evolve with redshift, (2) a fixed ratio between $f_{\rm star}$ and $f_{\rm gas}$ holds in a cluster at any radius and redshift. As we have shown here, both these assumptions are not valid in our simulated dataset whatever is the physics included in the simulations, in particular when considering the inner part of the clusters. Allen et al. (2004) use the simulation results by Eke et al. (1998) to fix $Y_{\rm b} = 0.824 \pm 0.033$ at $r \approx R_{2500}$ for their sample of *Chandra* exposures of the largest relaxed clusters with redshift between 0.07 and 0.9. We notice, for instance, that, while this value is in agreement with our simulation results at $z = 0$ in the runs with *Gravitational heating only* ($Y_{\rm b} = 0.82 \pm 0.06$), it is definitely lower than what we estimate at higher redshift (e.g. $Y_{\rm b} = 0.86, 0.89, 0.91$ at $z = 0.3, 0.7, 1$, respectively). This increase of $Y_{\rm b}$ with redshift is the consequence of the different accretion pattern of shock-heated baryons at different epochs. At later times, accreting gas had more time to be pre-shocked into filaments. As a consequence, they have a relatively higher entropy, thus relatively increasing the radius (in unit of the virial radius) where accretion shocks take place.

Since the tighter cosmological constraints provided by the cluster gas fraction alone are on $\Omega_{\rm m}$ (of the order of 16 per cent at 1σ level; e.g. Allen et al. 2004), we try to quantify the effect of the variation of the baryonic components with the radius and the redshift on this estimate. To this purpose, we use equation 1 and evaluate first how $\Omega_{\rm m}$ changes by varying $Y_{\rm b}$. The increasing baryon fraction with redshift induces larger estimate of $\Omega_{\rm m}$ with respect to what obtained from local measurements of $Y_{\rm b}$:

$$\frac{\Omega'_{\rm m} - \Omega_{\rm m}}{\Omega_{\rm m}} = \frac{\Delta\Omega_{\rm m}}{\Omega_{\rm m}} = \frac{Y_{\rm b}(< R_\Delta, z = z_o)}{Y_{\rm b}(< R_\Delta, z = 0)} - 1 \qquad (2)$$

is $+0.09$ at $R_\Delta = R_{2500}$ and $z_o = 0.7$ for the case with gravitational heating only and $+0.11$ at $z_o = 1$. (Here the prime symbol $'$ indicates the corrected value with respect to the reference one). Using instead the runs with reduced viscosity, the deviation decreases to about $+0.05$. As for the radiative runs, the bias is of the order of 20 per cent, that reduces to 2 per cent in presence of strong winds at $z = 1$. When outer cluster regions are mapped (i.e. $r \sim R_{500}$), the deviation converges to similar amounts due to the limited impact of cooling and feedback over large volumes: variations between $+0.03$ (weak winds) and $+0.10$ (strong winds) become comparable to $\Delta\Omega_{\rm m}/\Omega_{\rm m} \approx +0.08$ as measured in non–radiative runs.

A further contribution to the uncertainties comes from the dependence upon the radius and redshift of the ratio $f_{\rm star}/f_{\rm gas}$. In the observational determination of the baryon fraction from Eq. 1, this quantity is generally assumed to be 0.16, as measured in the Coma cluster within the virial radius (e.g. White et al. 1993). Note that our estimate from Lin et al. (2003) and adopting the total mass measurements in Arnaud et al. (2005) is 0.11 ± 0.04 or $M_{\rm gas}/M_{\rm star} \approx 8.7$ (r.m.s. $= 2.7$) at R_{500} in systems with gas temperatures larger than 3 keV. The latter value is a factor between 2.5 and 6 larger than what obtained in our simulated objects, thus witnessing the presence of significant overcooling. If we compare the ratio $\phi = f_{\rm star}/f_{\rm gas}$ measured for a Coma–like simulated cluster at R_{200} and

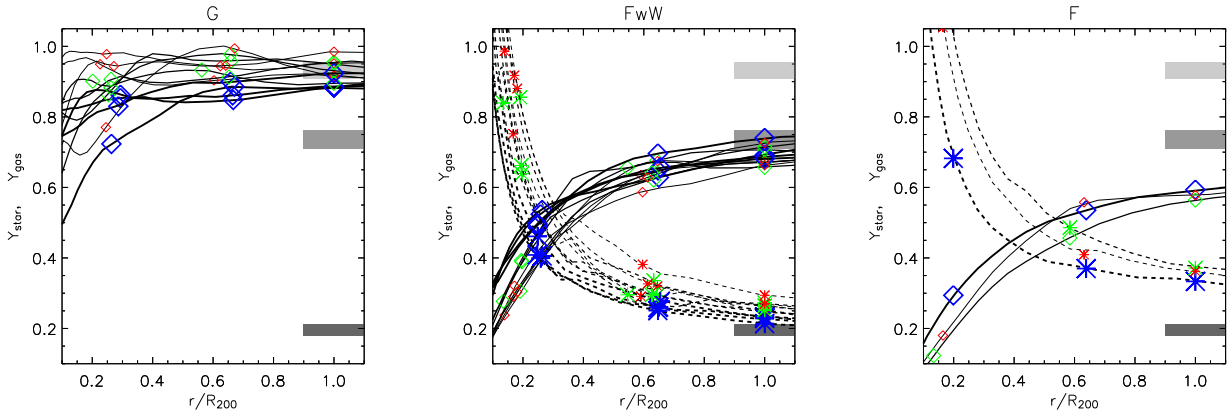

Figure 3. The comparison between the outputs of 3 different physical schemes out of the 6 investigated. The gas (solid line) and stellar (dashed line) mass fractions, normalized to the cosmic value, are plotted at $R_{2500}(\approx 0.3R_{200})$, $R_{500}(\approx 0.7R_{200})$ and R_{200}. Their evolution with redshift is indicated by the thickness of the lines (from thickest line/larger symbols to thinnest line/smaller symbols: $z = 0,\ 0.7,\ 1$). The shaded regions indicate the 1σ range of $Y_{\rm star}$, $Y_{\rm gas}$ and $Y_{\rm b}$ measured at R_{200} and $z = 0$ for the cluster set extracted from the cosmological box.

$z = 0$ with the estimates at other redshifts ($z_o = 0.7$ and 1; see, e.g., Fig. 3), we evaluate from equation 1

$$\frac{\Omega'_{\rm m} - \Omega_{\rm m}}{\Omega_{\rm m}} = \frac{\Delta\Omega_{\rm m}}{\Omega_{\rm m}} = \frac{1 + \phi(< R_\Delta, z = 0)}{1 + \phi(< R_\Delta, z = z_o)} - 1\,, \quad (3)$$

that is about -0.05. When $\phi = f_{\rm star}/f_{\rm gas}$ measured locally at R_{2500} is compared with the corresponding value at different redshifts, the deviation ranges between -0.74 (when winds are excluded) and -0.38 (when strong winds are present), whereas it is about -0.10 at R_{500}.

As for the runs with gravitational heating only the effect of the variation of $Y_{\rm b}$ with redshift and overdensity implies $\Delta\Omega_{\rm m}/\Omega_{\rm m} < +0.11$, thus comparable to the current statistical uncertainties from *Chandra* observations of the massive clusters out to $z = 1.3$ (Ettori et al. 2003, Allen et al. 2004). However, when the extra-physics of the radiative runs is included, $\Delta\Omega_{\rm m}/\Omega_{\rm m}$ has two contributions of $\approx +0.10$ and < -0.05, due to an increase with redshift of (1) $Y_{\rm b}$ (see Fig. 2) and (2) the stellar to gas mass fraction ratio (see Fig. 3). Both these effects are caused by a more efficient star formation in high redshift clusters.

In general, our results indicate that it may be dangerous to use simulations to calibrate observational biases for precision determination of cosmological parameters from the gas fraction in clusters. Although none of our simulation models includes a fair description of the actual ICM physics, it is interesting that different models provide different redshift–dependent corrections for the estimate of the cosmic baryon fraction from observations of the gas and star density distribution within clusters. If applied to observational data, such corrections would induce sizeable differences in the determination of the matter and dark energy density parameters.

ACKNOWLEDGMENTS
REFERENCES

[1] Allen S.W. et al., 2004, MNRAS, 353, 457

[2] Arnaud M., Pointecouteau E., Pratt G.W., 2005, A&A, 441, 893

[3] Borgani S. et al., 2004, MNRAS, 348, 1078

[4] Eke V.R. et al., 1998, ApJ, 503, 569

[5] Ettori S., Fabian A.C., 1999, MNRAS, 305, 834

[6] Ettori S., De Grandi S., Molendi S., 2002, A&A, 391, 841

[7] Ettori S., 2003, MNRAS, 344, L13

[8] Ettori S., Tozzi P., Rosati P., 2003, A&A, 398, 879

[9] Gardini A. et al., 2004, MNRAS, 351, 505

[10] Kirkman D. et al., 2003, ApJS, 149, 1

[12] Lin Y.T., Mohr J.J., Stanford S.A., 2003, ApJ, 591, 749

[12] Mazzotta P. et al., 2004, MNRAS, 354, 10

[13] Navarro J.F., Frenk C.S., White S.D.M., 1995, MNRAS, 275, 720

[14] Rasia E., Tormen G., Moscardini L., 2004, MNRAS, 351, 237

[15] Springel V., Hernquist L., 2003, MNRAS, 339, 289

[16] Springel V., 2005, MNRAS, in press (astro-ph/0505010)

[17] Tormen G., Bouchet F.R., White S.D.M., 1997, MNRAS, 286, 865

[18] White S.D.M. et al., 1993, Nature 366, 429